

Metal–Organic Gels Based on a Bisamide Tetracarboxyl Ligand for Carbon Dioxide, Sulfur Dioxide, and Selective Dye Uptake

Dennis Dietrich,[†] Christopher Licht,[‡] Alexander Nuhnen,[†] Simon-Patrick Höfert,[†] Laura De Laporte,^{‡,§} and Christoph Janiak^{*,†,§}

[†]Institut für Anorganische Chemie und Strukturchemie, Heinrich-Heine-Universität Düsseldorf, Universitätsstraße 1, 40225 Düsseldorf, Germany

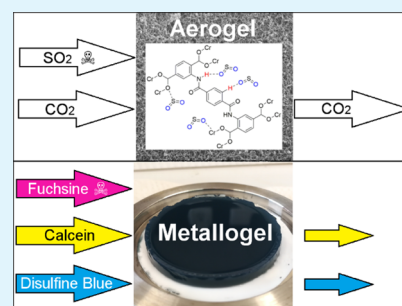
[‡]DWI—Leibniz Institute for Interactive Materials, Forckenbeckstraße 50, 52074 Aachen, Germany

[§]Hoffmann Institute of Advanced Materials, Shenzhen Polytechnic, 7098 Liuxian Blvd, Nanshan District, Shenzhen 518055, China

Supporting Information

ABSTRACT: A metal–organic gel (metallogel) based on the new tetracarboxyl ligand N^1,N^4 -(diterephthalic acid)terephthalamide in combination with chromium(III) has been converted into its xero- and aerogel and demonstrated to have excellent specific sorption properties for dyes in its metallogel state, where fuchsine is adsorbed faster than the two other dyes, calcein and disulfine blue, and for water, sulfur dioxide and carbon dioxide in its xero- and aerogel state. The metallogel showed very good shape retention and could be extruded from molds in designed shapes. In a rheology experiment, the storage modulus was determined to be 1440 Pa, and the metallogel is elastic up to 3 Hz, breaking at strains higher than 0.3%. Additional metallogels utilizing the same ligand with a wide range of metal ions (Al(III), Fe(III), Co(III), In(III), and Hg(II)) have also been synthesized, and the aluminum and mixed aluminum–chromium derivative were also converted into its aerogel. The highly porous Cr, Al, and AlCr metal–organic aerogels proved stable against water vapor in a physisorption experiment and were used to model breakthrough curves for SO_2/CO_2 gas mixtures with the idealized adsorbed solution theory from their physisorption isotherms. The breakthrough simulation utilized SO_2/CO_2 equivalencies from a real world application and showed effective retention of SO_2 from the gas mixture. Furthermore, the materials in this work exhibit the highest SO_2 uptake values for metal–organic aerogels so far (up to $116.8 \text{ cm}^3 \text{ g}^{-1}$, or 23.4 wt %).

KEYWORDS: metallogel, metal–organic aerogel, xerogel, amide-functionalized linker, sulfur dioxide sorption, gas sorption, dye sorption



INTRODUCTION

Porous metal–organic frameworks (MOFs) with high surface areas and potential applications in gas storage and purification, catalysis, drug delivery, and pollutant sequestration¹ are a current field of high interest.^{2–7} The properties of MOFs can be tuned toward their respective applications, through various modifications of the organic linker or the metal nodes.^{8–10} As MOFs are most commonly available as crystalline powders, shaping with retention of porosity is a critical issue. By embedding MOFs into different types of polymers to yield xerogels and aerogels, it is possible to tailor these composite systems into shapes suitable to the application without losing much of the physisorption properties.^{11–14}

Aerogels are amorphous solids with low density, which, when properly dried, can possess high accessible surface areas. On their way to becoming an aerogel, the material usually starts out as a solution, or sol, which is then processed to form a gel. Within the gel, a solid-like network immobilizes the liquid-like phase, typically the solvent, through capillary forces and solvent–gelator interactions.¹⁵ Removal of all swelling agents without suppressing the capillary forces within the gel

produces a xerogel, often accompanied by a collapse of the micropores in the solid-like network. The xerogels may sometimes retain their mesopores, and surface areas can even be comparable to those of the subsequent aerogels.¹⁶ If the swelling agent is removed under supercritical conditions, the capillary forces are suppressed, preventing pore collapse and leading to a highly porous solid with low density and high surface area called aerogel. Aerogels can also be formed if the network in the gel is strengthened enough to withstand evaporation of the solvent.^{17,18} Common types of aerogels are of organic nature, either as polymers or as pure carbon aerogels, with the precursor to the carbon aerogels often being an organic aerogel, or of metal-oxide nature, including silica and metal oxide aerogels.¹⁹ Their applications also include gas storage and separation as well as catalysis, but also thermal or acoustic insulation.^{20–22}

Received: March 15, 2019

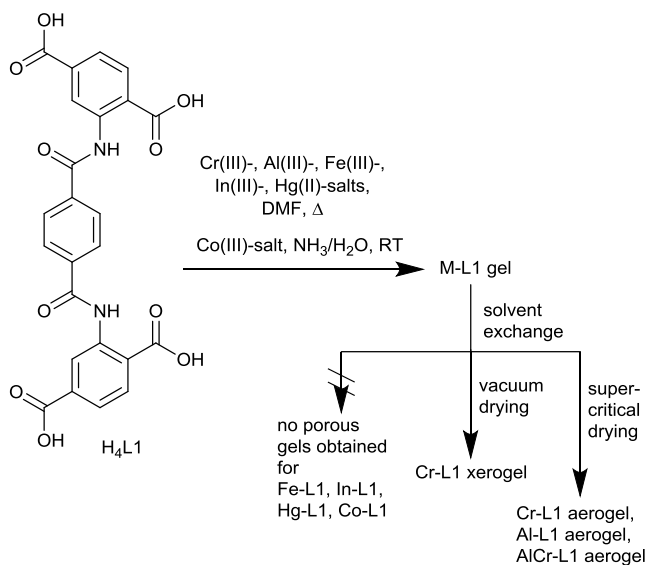
Accepted: May 7, 2019

Published: May 7, 2019

In 2009, Kaskel et al. bridged the gap between MOFs and aerogels by synthesizing a metal–organic aerogel (MOAG) based on Fe-1,3,5-benzene tricarboxylate with a surface area above $1600 \text{ m}^2 \text{ g}^{-1}$.²³ As a first step, a metallogel based on coordination chemistry is formed. These metallogels readily exhibit interesting properties in applications and have been shown to respond to a variety of thermal and chemical stimuli.²⁴ The easy processability of these gels allows them to be used in many industrial fields, including drug delivery, gas storage, and optoelectronics, omitting the embedding often required for metal–organic frameworks.²⁵ Afterward, the aerogel is formed by supercritical drying of the metallogel, and the coordination bonds between the linker and the metal nodes can be observed by infrared (IR) spectra. In recent times, the interest in MOAGs has grown. MOAGs have been used for dye uptake, microcystin removal from water, solid-phase microextraction, and electrocatalytic reduction.^{26–29} The use of porous metal–organic compounds for flue-gas desulfurization is currently investigated and discussed as a highly interesting class of materials.^{30,31} As a minor constituent of flue gas, up to 95% of sulfur dioxide can be removed using limestone as chemical absorbent.^{32,33} The remaining 5% of SO_2 is the major contributor to the 80 Mt of worldwide SO_2 emissions from energy-related sources in 2015, which represents a significant effect on the health of humans and on the environment.^{34–36}

In this work, we present a bisamide tetracarboxyl ligand (Scheme 1), which readily forms metallogels with a variety of

Scheme 1. Bisamide Tetracarboxyl Linker Used in Metal–Organic Gel Synthesis and Overview on the Syntheses and Gel Products



metal ions. The resulting metallogels have been converted to xero- and aerogels, by exchanging the solvent and vacuum drying for the xerogels or supercritical removal of the solvent for the aerogels, and have been characterized in terms of their porosity using N_2 , CO_2 , and Ar physisorption and gas uptake capacity. The analyzed gases include CO_2 , H_2O , and SO_2 , as they should show enhanced interaction with the functional amide groups present in the linker of the MOAGs. Furthermore, the metallogel based on chromium showed selective uptake of dyes from aqueous solution. To the best of

our knowledge, there were, so far, no reports on chromium- or aluminum-based MOAGs for SO_2 sorption.

RESULTS AND DISCUSSION

Ligand and Gel Synthesis. The ligand N^1, N^4 -(diterephthalic acid)terephthalamide, $\text{H}_4\text{L1}$, was synthesized from 2-aminoterephthalic acid and terephthaloyl chloride in water with the addition of excess potassium carbonate in good yields. A single crystal X-ray structure analysis of $\text{H}_4\text{L1}$ after recrystallization from dimethylformamide (DMF) confirmed the ligand configuration (Figure 1).

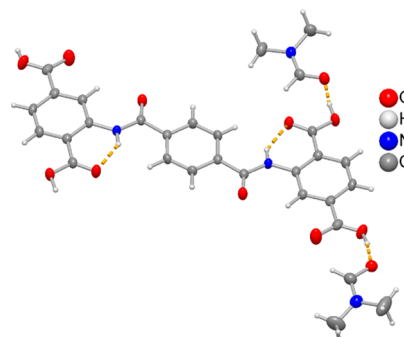


Figure 1. Molecular structure of $\text{H}_4\text{L1}$ with two of the four hydrogen-bonded DMF molecules in $\text{H}_4\text{L1}\cdot 4\text{DMF}$ (70% thermal ellipsoids, H atoms with arbitrary radii). The resolved DMF disorder is not shown for clarity. For further crystallographic details and information on hydrogen-bonding, see Tables S1, S2 and Figure S1, Supporting Information. The structural data have been deposited with the Cambridge Crystallographic Data Center (CCDC no. 1889949).

The chromium(III), aluminum(III), iron(III), mercury(II), and indium(III) metallogels were synthesized from their nitrate salts, with the exception of mercury, where the acetate salt was used, and $\text{H}_4\text{L1}$ in a solvothermal reaction in DMF. Because of poor solubility of the ligand, the reaction mixture had to be heated to 80°C to dissolve the ligand. An attempt was made to dissolve the ligand in DMF at 80°C first, but the ligand stayed mostly insoluble without the addition of a metal salt. Adding various bases or acids to help dissolve the ligand in DMF usually prevented the metallogels from forming. The red iron and white indium metallogels were not homogeneous, as the gels already started to form while the ligand had not completely dissolved yet. Processing of Fe-L1 and In-L1 proved to be impossible, and these irregular metallogels were not investigated further. The white metallogel of mercury was formed by separately heating suspensions of $\text{H}_4\text{L1}$ in DMF and solutions of mercury acetate in DMF to 80°C and mixing the two. The mercury metallogel formed instantly and stays stable for a while before turning back into a liquid. Reheating the liquid did not reform the mercury metallogel. The same mixing procedure was also unsuccessfully tried on the iron and indium gel. The mercury metallogel has not been processed further due to the potential toxicity. The cobalt(III) metallogel was synthesized by dissolving $\text{H}_4\text{L1}$ and hexaamminecobalt chloride in 25% ammonia water before mixing the two solutions and letting the ammonia evaporate (see Supporting Information and Table S4 for synthetic details). The orange metallogel of cobalt could not be handled outside of its reaction vessel, as it did not prove to be stable enough to withstand the transfer to another vessel. This was most likely due to the inert nature and stability of the $[\text{Co}(\text{NH}_3)_6]^{3+}$ ion

(as indicated by the retention of its original orange color), which prevents formation of Co-L1 carboxylate linkages but instead gives a supramolecular $[\text{Co}(\text{NH}_3)_6]^{3+}\text{-H}_{4-n}\text{L1}^{n-}$ hydrogen-bonded gel structure. Altogether this left only the handleable chromium and aluminum metallogels and a mixed AlCr metallogel for further investigations. The different metallogels were repeatedly synthesized to ensure reproducibility. The gel constitution was qualitatively shown by the inversion test (Figure 2).



Figure 2. From left to right: Metallogel Cr-L1, AlCr-L1, Al-L1, Fe-L1, In-L1, Co-L1. All vessels are presented in an upturned state. A picture of Hg-L1 can be found in the Supporting Information (Figure S2).

The dark-green chromium metallogel showed excellent stability and were easily removed from their reaction vessels while retaining their shape (Figure 8). The white aluminum metallogels remained stable enough for further processing; however, handling them outside of moving them to the next reaction vessel usually resulted in the destruction of the metallogel.

From the metallogels the xerogels of chromium and aluminum were formed by removing the solvent in vacuo after exchanging DMF with ethanol while the aerogels were formed by first exchanging the DMF with ethanol followed by supercritical drying with CO_2 . The mixed chromium–aluminum metallogel AlCr-L1 was processed in the same way (see Experimental Section for details on solvent exchange and supercritical drying procedure). The successful DMF-to-ethanol solvent exchange was followed using IR techniques (Figure 3).

The infrared spectra of the aerogels of Cr-L1, AlCr-L1, and Al-L1 exhibited the disappearance of the major peaks caused by the carboxylic acid group at around $1650\text{--}1700$ and 1190 cm^{-1} . The appearance of new peaks at around 1425 and 1567 cm^{-1} indicate successful formation of the carboxylate (Figure 4). The characteristic absorption bands for the coordinated ligand at 1567 cm^{-1} correspond to the asymmetric stretching vibration (ν_{as}) and the band at 1425 cm^{-1} to the symmetric stretching vibration (ν_{s}) of the carboxylate group. The frequency gap ($\Delta\nu$) between these bands $\Delta\nu = \nu_{\text{as}}(\text{COO}^-) - \nu_{\text{s}}(\text{COO}^-)$ of 142 cm^{-1} reveals that the carboxylate ligation is in the bidentate bridging mode ($\mu_{1,3}$ - or $\eta^1:\eta^1:\mu_2\text{-M-O-C-O-M}$).^{37,38}

In common aerogel literature, the powder X-ray diffractometry (PXRD) patterns of gels derived from their respective metal–organic frameworks often show similar peaks. The reason given for this occurrence is due to the formation of metal–organic framework nanoparticles, where further coordination is perturbed, which then results in the formation of a gel.²⁶ In the materials of this work, no discrete peaks were visible in the PXRD patterns, suggesting that there might have been no such formation of nanostructures (Figure S10).

The IR spectra showed a bidentate bridging of the ligand and the PXRD patterns lacked discrete peaks and only suggested a certain long-range order through the broad bands.

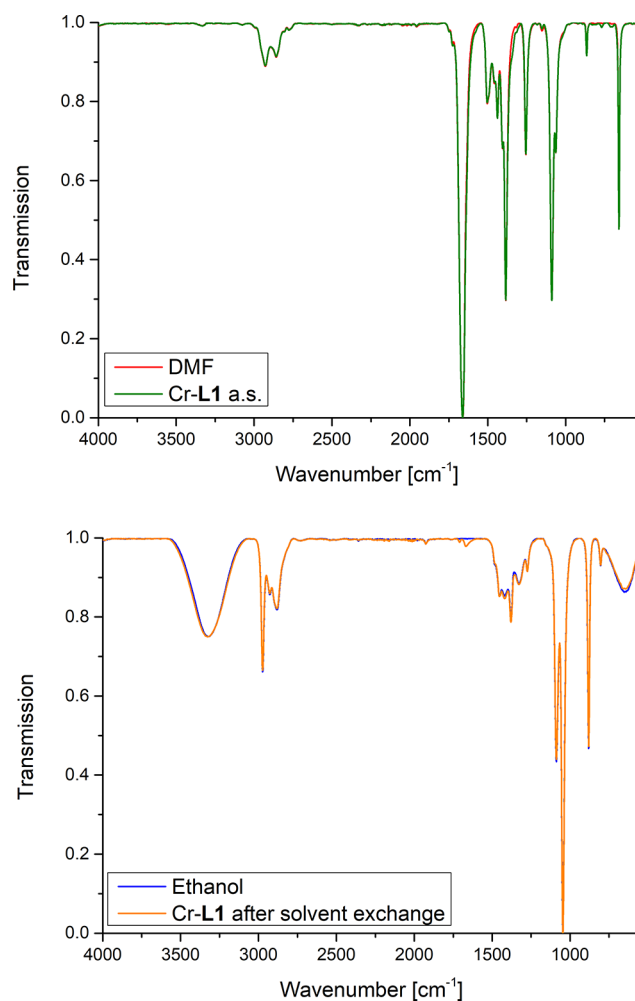


Figure 3. Exemplary infrared spectra of the metallogel Cr-L1. The solvent spectra dominate, as even the gels with the lowest amount of solvent are still made up of over 96 wt % solvent (for Cr-L1 as synthesized, a.s.). Top: Spectrum of Cr-L1 as synthesized superimposed with the spectrum of pure DMF. Bottom: Spectrum of Cr-L1 after solvent exchange with ethanol superimposed with the spectrum of neat ethanol.

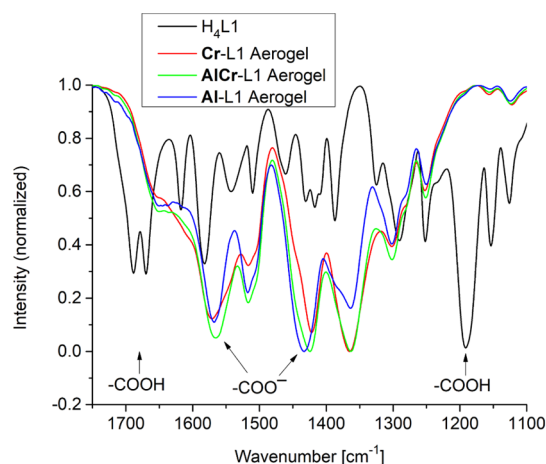


Figure 4. IR spectra from L1 and the respective aerogels. The carboxylic acid bands at $1650\text{--}1700\text{ cm}^{-1}$ and at 1191 cm^{-1} in the spectrum of L1 vanish in the aerogel spectra, and new bands, which can be attributed to carboxylate vibrations, appear instead.

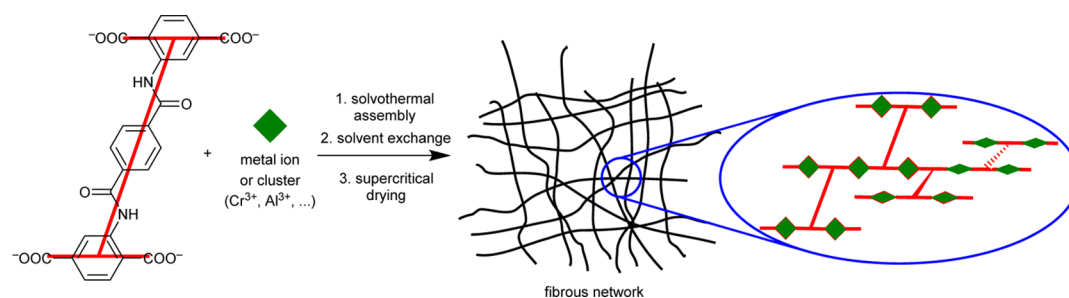


Figure 5. Schematic synthesis procedure of metal–organic gel formation. For the metal unit (green), an octahedral coordination sphere is assumed where at least two carboxylate groups of the tetratopic linker (red) are cis- or trans-coordinated. The resulting coordination polymer chains can be interlinked in three dimensions and are randomly oriented. The gel is formed through supramolecular interactions of the solvent with the coordination polymer chains. The resulting fibrous network randomly propagates in multiple directions.

In the metal–organic gel literature, one-dimensional infinite metallogelators are often reported.^{39–41} Here, the ligand H₄L1 allows for coordination of four metal ions.

For the microstructure of the Cr- and Al-organic gels, we assume the metal atoms with their typical octahedral coordination environment. Irrespective if the metal building units are monometallic or form a polynuclear hydroxido-bridged metals chains as in MIL-53(Cr, Al)^{42,43} and most Al-MOFs (CAU-10-H,⁴⁴ Al-fumarate⁴⁵), the tetratopic flexible ligand can then link these metal units to an up to three-dimensional structure. The metal and linker groups can readily incorporate solvent molecules in a second-sphere coordination through coordination and hydrogen bonding. Further solvent molecules then fill the voids. Because of the flexible nature of the linker, the metal–ligand structure is unlikely to be crystalline but forms an amorphous metal–organic gel (Figure 5). In the current metal–organic gel literature, the microstructures are often based on “educated guesses”, especially when the structure is not derived from a known metal–organic framework.^{46,47}

Where possible, the morphology of the xero- and aerogels has been analyzed by scanning electron microscopy (SEM) and transmission electron microscopy (TEM). Fibrous networks with pore-like voids could be observed for the aerogels of Cr-L1, Al-L1, and AlCr-L1. The xerogel of Cr-L1 showed a rough surface with potential porosity (Figure 6). The xerogel of Fe-L1 appeared as smooth and without distinctive surface features at all magnifications. The xerogels of Co-L1 and In-L1 had no directly visible pores and appeared to be consisting of unconnected fibers (Figure S10). SEM–energy dispersive X-ray spectroscopy (SEM–EDX) analyses reveal through the metal element mapping a homogenous distribution of metal atoms throughout the metal–organic gel materials (Figures S5–S8, Supporting Information).

Rheological Experiments. Rheological measurements have been performed in order to investigate the mechanical properties of Cr-L1. The metallogels are preformed in a round-shaped mold of stainless steel by heating at 100 °C for 24 h (Figure 7a). After gelation, the metallogels are carefully moved to the rheometer plate (Figure 7b). In the case of Al-L1 and AlCr-L1, the metallogels were too fragile for transfer to the rheometer. Both amplitude and frequency sweeps were performed, revealing a storage modulus of 1440 ± 139 Pa for the Cr-L1 gel. The metallogel is elastic up to 3 Hz and starts to break at strains higher than 0.3% (Figure 7c,d).

Shaping. The rheological behavior of the metallogels also influenced their shapeability. The metallogels can be casted into various forms, but without additional support only the Cr-

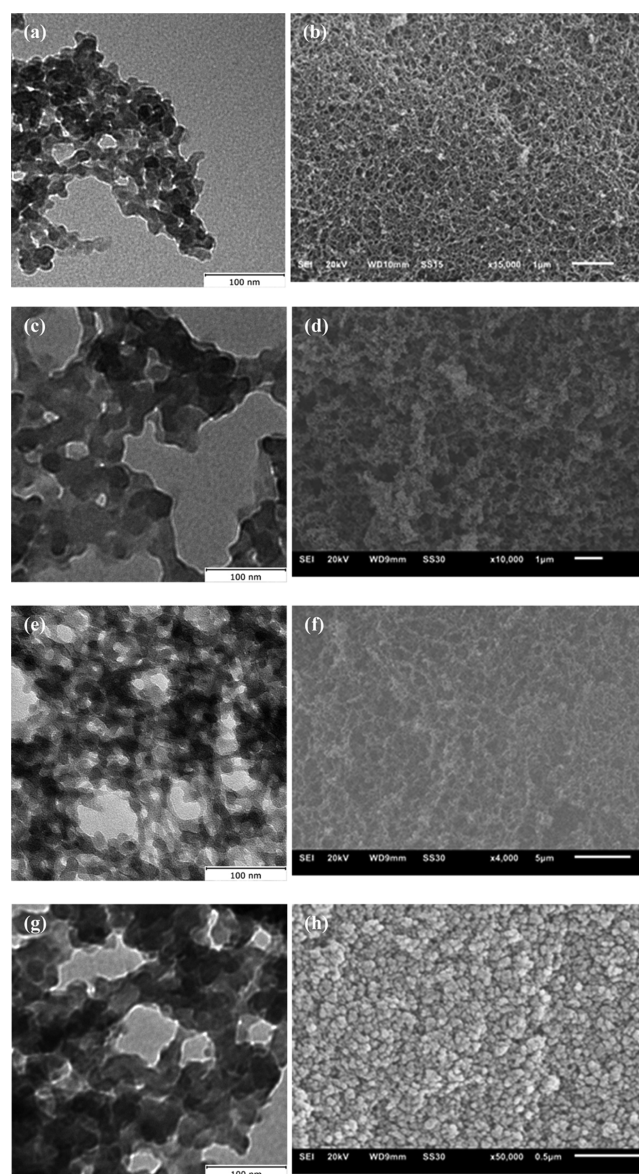


Figure 6. TEM and SEM micrographs of the aerogels of Cr-L1 (a/b), Al-L1 (c/d), and AlCr-L1 (e/f) and the xerogel of Cr-L1 (g/h).

L1 metallogel was able to maintain its shape outside of its reaction vessel (Figure 8). It was possible to cast Cr-L1 into complex shapes, which were stable as long as solvent evaporation was prevented.

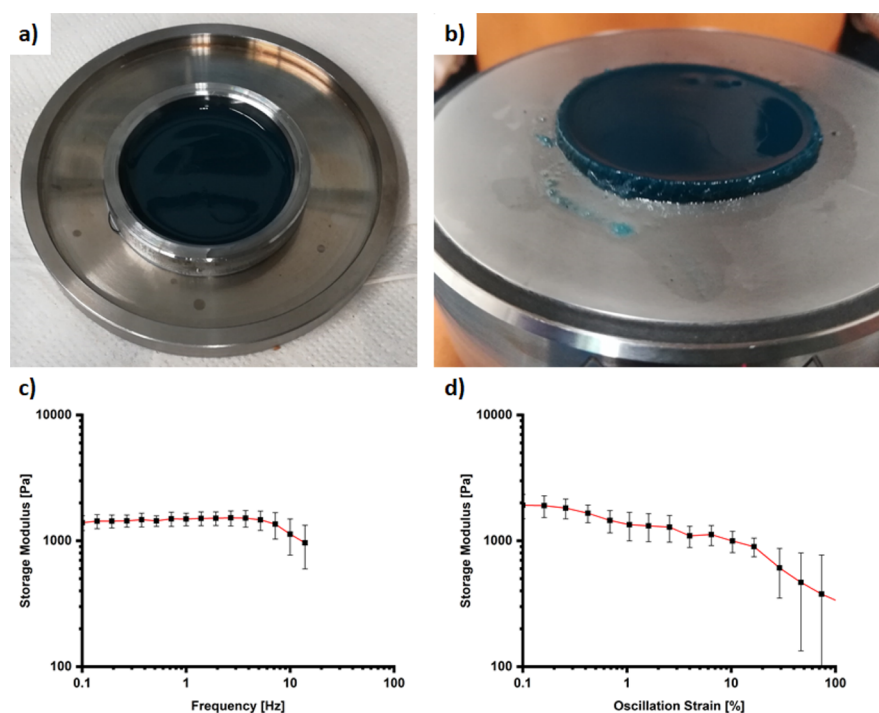


Figure 7. Cr-L1 metallogel in a ring of stainless steel after 24 h at 100 °C (a) and subsequent placing onto the rheometer plate (b). Axial force controlled rheology measurements (c,d) show the average storage modulus during a frequency (strain set at 0.3%) and amplitude (frequency set at 0.5 Hz) sweep, respectively.



Figure 8. Metallogels of Cr-L1, AlCr-L1, and Al-L1 in “wet” and dry states. Left: Cr-L1 (dark green), AlCr-L1 (light green), and Al-L1 (colorless) as poured directly from a cylindrical vessel. Shape retention for the mixed metal AlCr-L1 metallogel is poor, while the Al-L1 metallogel does not maintain its shape at all. Middle: Aerogel and xerogel pieces of Cr-L1, AlCr-L1, and Al-L1. Right: Cr-L1 cast into a shape with a total volume of 32 mL. Tin foil can be seen on top which was added to alleviate a suction problem when removing the metallogel from its cast.

Dye Uptake. The stable metallogels of Cr-L1 and AlCr-L1 show potential applications in wastewater treatment. Dye uptake studies from aqueous solution have been carried out with fuchsine, a red cationic dye which is listed as an IARC Group 2B carcinogen (“possibly carcinogenic to humans”), calcein, a yellow and fluorescent neutral dye, and disulfine blue VN 150 (or Acid Blue 1), a blue anionic dye.⁴⁸ The Cr-L1 metallogel shows high uptakes for all three dyes. Upon reaching adsorption equilibrium, 1 mL of the Cr-L1 metallogel is capable of completely removing fuchsine from 2 mL of a dye solution with a concentration of 100 mg L⁻¹. Furthermore, the equilibrium for calcein sorption is reached within 24 h (Figures 9 and 10). The AlCr-L1 metallogel is also capable of taking up fuchsine and disulfine blue VN 150, although not as thoroughly as the Cr-L1 metallogel (Figure 9). For calcein, the measurements with gels containing Al are unreliable, as the dye is known to form inter alia with Al³⁺ soluble Al-calcein complexes which lead to quenching or shifts in the absorption spectrum.⁴⁹ Determinations of dye uptake were not possible with the Al-L1 metallogel in general, as the gel breaks apart upon adding the dye solutions.

Dyes are frequently used in the biosciences for labeling reactions. Removing excess dye after a labeling reaction is often difficult and time-consuming but is essential for accurate determination of dye-to-protein ratios. We point to a kit sold by Thermo Scientific as “Pierce Dye Removal Columns” to effectively bind to unconjugated fluorescent dye molecules, such as calcein, from protein solutions to rapidly purify fluorescent conjugated antibodies and other proteins after labeling reactions. These fluorescent dye removal columns enable fast and efficient removal of nonreacted fluorescent dyes from protein labeling reactions.⁵⁰

Further, the dyes are a model system to show selective uptake of large molecules with different charges. In general, the removal of dyes from wastewater is of industrial interest, to mitigate the potential effects on the aquatic environment.^{51,52} The only problematic among the three dyes tested here, which is to be removed from wastewater is the carcinogenic fuchsine.

The specific fuchsine uptake in the Cr-L1 metallogel is greater than 200 mg g⁻¹, as the density of the metallogel approaches 1 g cm⁻³ and 1 mL of metallogel was capable of removing 0.2 mg fuchsine from 2 mL of water. The specific

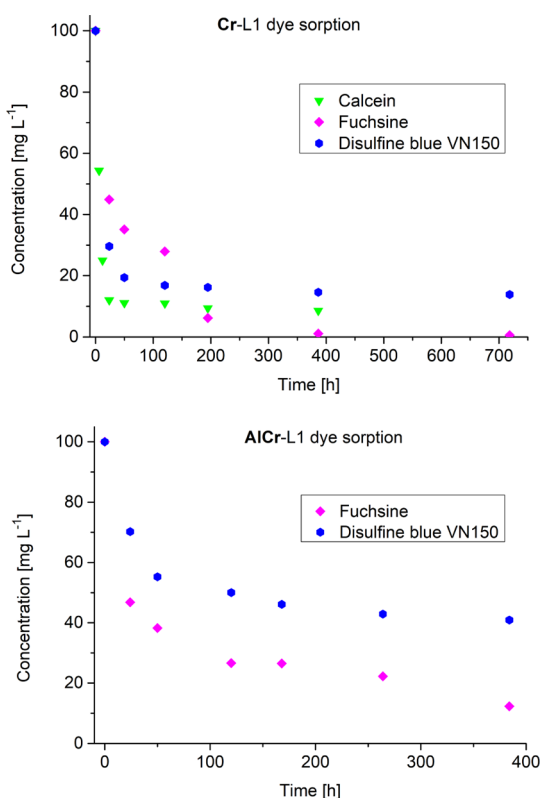


Figure 9. Sorption performance of 1 mL of Cr-L1 and AlCr-L1 metallo gels for 2 mL of different dye solutions with a concentration of 100 mg L⁻¹ each.



Figure 10. Metallo gels with dye solutions as prepared and used for UV experiments. The uptaken vessels show the retained gel state of the samples. Top: Dye uptake after 7 days. Bottom: Dye uptake after 1 month. The fuch sine dye has been almost completely absorbed, while calcein and disulfine blue VN150 partially remain in solution.

uptake capacity of the AlCr-L1 metallo gel is 176 mg g⁻¹. Comparison with materials in the literature suggests acceptable uptakes of basic fuch sine to the point that the metal-organic gel materials are outperforming the reported fuch sine sorbents in the literature (Table 1).

Possible explanations for the high dye uptakes include certain interactions of the cationic tertiary amine groups,

Table 1. Basic Fuch sine Uptake of Different Materials in the Literature

material	uptake capacity [mg g ⁻¹]	ref
Cr-L1 metallo gel	>200	this work
AlCr-L1 metallo gel	176	this work
calcined mussel shell	141.65	53
epichlorohydrin cross-linked peanut husk	116.28	54
mesoporous carbon C-KS	10.66	55
ceramic microsphere gangue	24.16	56
bottom ash	91.56	57
deoiled soya	134.81	57

present in disulfine blue VN150 and fuch sine, with carboxylates and carboxylic acid groups of the ligand in the metallo gel network. These interactions include Yoshida H-bonding between the aromatic moieties of the dyes with hydrogen atoms of the carboxylates, n- π interactions between the nucleophilic lone-pair electrons in the dyes with the empty π^* orbitals of the carbonyl groups in the network, dipole-dipole H-bonding, and π - π interactions.⁵⁸ Calcein is a known chelator of transition metals and likely coordinates to unoccupied metal sites.

We have also tested the leaching or metal ion release from the gels through atomic absorption spectroscopy. Cr-L1 and AlCr-L1 gel (2 mL) were covered with 1 mL of water and left standing for 5 days. The accumulated amount of released Cr ions for the Cr-L1 metallo gel was 0.47 mg L⁻¹, while the accumulated amounts of released Al and Cr ions for the AlCr-L1 metallo gel were below the detection limit (<0.01 mg L⁻¹).

Surface Area and Pore Constitution Analysis of the Aerogels and Xerogel. Aerogels are commonly associated with high accessible surface areas and the xerogels based on the same gel may sometimes retain the surface area while undergoing changes in pore constitution, as discussed in the Introduction. To determine the surface area and porosity, gas adsorption isotherms of CO₂ at 195 and 273 K, Ar at 87 K and N₂ at 77 K have been measured (Figures 11 and S14–S16).

The Cr-L1 aerogel showed the highest Brunauer–Emmett–Teller (BET) surface area in the Ar physisorption experiments with a value of 609 m² g⁻¹, followed by the Cr-L1 xerogel (604 m² g⁻¹) and the aerogels of AlCr-L1 and Al-L1, (441 and 479 m² g⁻¹, respectively) (Table 2). Both Ar and N₂ physisorption experiments reveal type II isotherms with H3 hysteresis loops for the aerogels, which suggests that, in combination with the high surface areas, the materials are micro-, meso-, and macroporous. This assumption is in line with the results from the SEM and TEM micrographs (Figure 6). The xerogel exhibits a type IV isotherm with an H2b hysteresis loop, easily observed in both the N₂ and Ar physisorption isotherms, suggesting that the material is mainly mesoporous.

The different BET surface areas derived from Ar and N₂ sorption are due to the better micropore filling with the former. Argon as adsorptive at the boiling point temperature of liquid argon (87 K) fills micropores of dimensions 0.5–1 nm at higher relative pressures p/p_0 of 10⁻⁵ to 10⁻³ compared to nitrogen at 77 K ($p/p_0 = 10^{-7}$ to 10⁻⁵), which leads to accelerated diffusion and equilibration processes for argon. Further, argon does not have a quadrupole moment, unlike N₂ (4.7 cm²). Because of its quadrupole moment, the orientation of an N₂ molecule depends on the chemical surface structure of the adsorbent, so that specific quadrupole interactions of N₂ to

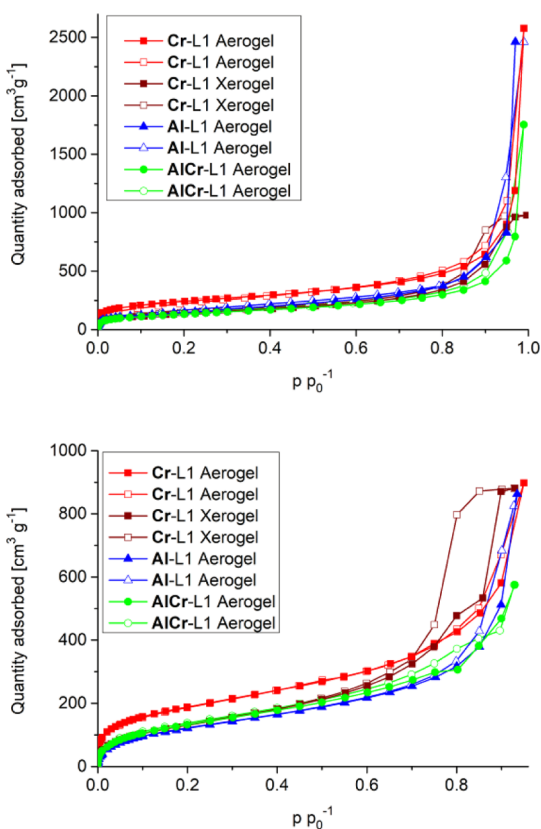


Figure 11. Adsorption (filled symbols) and desorption (empty symbols) for N_2 at 77 K (top) and Ar at 87 K (bottom) for the aerogels of compounds Cr-L1 aerogel (red squares), Cr-L1 xerogel (brown squares), Al-L1 (blue triangles), and AlCr-L1 (green circles). Full range Ar isotherms can be found in the Supporting Information (Figure S16).

Table 2. Surface Area and Porosity Analysis of Aero- and Xerogels from Ar, N_2 , and CO_2 Sorption Data

compound	$S_{BET, Ar}$ at 87 K [$m^2 g^{-1}$] ^a	S_{BET, N_2} at 77 K [$m^2 g^{-1}$] ^b	$V_{tot,3} (Ar)$ [$cm^3 g^{-1}$] ^c	$V_{tot,3} (N_2)$ [$cm^3 g^{-1}$] ^d	$V_{micro, (CO_2)}$ [$cm^3 g^{-1}$] ^e
Cr-L1 aerogel	609	860	1.90	1.58	0.049
Cr-L1 xerogel	604	503	1.20	1.44	0.030
AlCr-L1 aerogel	441	480	0.69	1.21	0.036
Al-L1 aerogel	479	523	1.01	1.82	0.044

^aSurface area was derived from the BET plot mostly in the p/p_0 range 0.08–0.25. ^bSurface area was derived from the BET plot in the p/p_0 range of mostly 0.10–0.20. ^cTotal pore volume at $p/p_0 = 0.95$ for pores ≤ 20 nm. ^dTotal pore volume at $p/p_0 = 0.95$ for pores ≤ 20 nm. ^ePore volume for pores with $d \leq 1$ nm (10 Å) from the NLDFT calculations with a “ CO_2 on carbon, slit pores” model at 273 K.

the adsorbent can falsify the measurement by about 20%. In summary, the adsorptive argon is seen as less sensitive to artifact differences in the structure of the adsorbent surface than nitrogen and is now recommended as an alternative adsorptive for surface area determination.⁵⁹

As a downside, kinetic restrictions do not allow Ar to be used for the determination of very narrow micropores.⁵⁹ CO_2 physisorption at 273 K offers the benefits of accelerated diffusion of the analysis gas and therefore allows for

determination of even the narrowest micropores with $d \leq 1$ nm (10 Å). The transition from metallo- to xerogel is often accompanied by a collapse of the micropores in the resulting xerogel network.¹⁶ Thus, it is remarkable that the micropores of the xerogel of Cr-L1 did not completely collapse by the capillary forces acting upon the material during the vacuum drying process. Still, the micropore volume is lower than in the aerogels, which were obtained under supercritical drying conditions suppressing the capillary forces to prevent pore collapse.

All aerogels show the expected wide pore size distribution, while the xerogel of Cr-L1 shows a narrower pore size distribution (Figure 12). We note that the BET method based

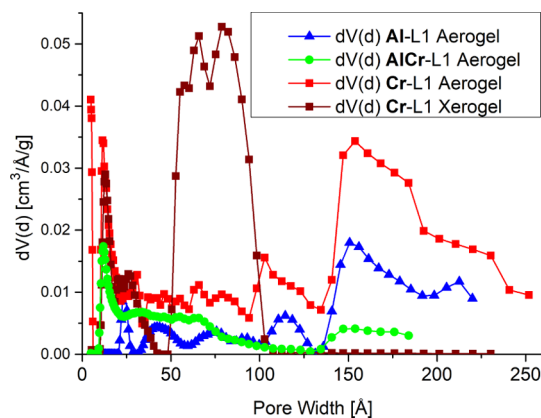


Figure 12. Pore size distribution curves of the aerogel materials and the xerogel obtained from Ar physisorption isotherms at 87 K and quenched solid-state density functional theory (QSDF) calculations (“Ar on carbon, slit pore” model, except for the Al-L1 aerogel, where an “Ar on carbon, cylindrical pore” model was used). Pores sizes up to ~ 200 Å are addressed. The pore widths of the aerogels are distributed over the whole range, while the xerogel does not exhibit pores wider than 100 Å in the addressed range.

on Ar and N_2 adsorption addresses micropores (pores < 20 Å, 2 nm) and mesopores smaller than ~ 200 Å (20 nm; at $p/p_0 = 0.95$) out of the full mesopore range up to 500 Å (50 nm). The similarity in porosity between the aerogels of Cr-L1 and Al-L1 is quite obvious, and their main difference is the lower total pore volume for the Al-L1 aerogel (Table 2, Figure S18). The major contribution to the pore volume is found in the range above 140 Å of pore width for these two aerogels (Figure S18). As a result, the metal ion does not seem to influence the general pore constitution other than changing the total volume. For the xerogel of Cr-L1, porosity was retained, as was already shown by the above physisorption experiments. The pore size distribution is different to the aerogels, with more than 80% of the total pore volume in the relevant range stemming from pores in the range of 50–100 Å (Figure 12).

It is evident that stable aerogels of Cr-L1, Al-L1, and AlCr-L1 and a xerogel of Cr-L1 could be obtained with permanent micro- and mesoporosity. Pore volumes for MOAGs containing Cr or Al extend over a wide range of 0.067–4.5 $cm^3 g^{-1}$ (Table S9).^{26,27,46,47,60} The literature suggests that a majority of those aerogels exhibit pore volumes between 1 and 2 $cm^3 g^{-1}$, and thus the pore volumes of the Cr- and Al aerogels from this work compare well to the pore volumes of typical aero- and xerogels in the literature.

Uptake of H_2O Vapor and Gases CO_2 and SO_2 . Cr- and Al-MOFs have been shown to be hydrothermally among the

most stable MOFs.^{61,62} Hence, the porous Cr- and Al-gels have been tested for their H₂O uptake at 20 °C (Figure 13) and

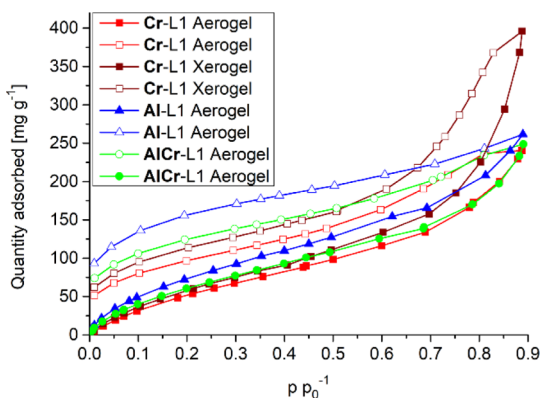


Figure 13. Water sorption isotherms of the xero- and aerogels. The isotherms show an onset of pore condensation effects at high p/p_0 and a large hysteresis, the latter suggesting prominent interactions between H₂O and the framework.

their CO₂ and SO₂ uptakes at different temperatures (Figure 14). The water sorption isotherms show no special behavior and pore condensation is visible at larger partial pressures. A large desorption hysteresis for all materials and the adsorptives H₂O and SO₂ is indicative of their strong interactions with the network. The H₂O desorption isotherm only closes at very low

pressure. The SO₂ sorption isotherms exhibit pore condensation at all three measured temperatures. For SO₂ especially strong interactions are observed through the large hysteresis for materials containing Al, while the hystereses for the Cr materials are generally smaller. This behavior transfers to the CO₂ sorption isotherms. When comparing uptake performance, the Al-L1 aerogel has the highest uptake of SO₂ and H₂O (before onset of pore condensation) and the lowest uptake of CO₂, suggesting that this material preferably forms strong bonds with highly polar gases. The presence of Cr in the networks of the other materials seemingly disturbs this preference, as the mixed-metal material AlCr-L1 falls more in line with the Cr-L1 aero- and xerogel in terms of uptake performance, although larger hystereses are still observed when Al is present.

For MOFs, a variety of interactions with sulfur dioxide have been elucidated, which act together to enhance its adsorption. Modeling calculations, in situ powder X-ray diffraction, inelastic neutron scattering, and infrared studies on SO₂ in MOFs have revealed interactions of sulfur dioxide by hydrogen bonding to hydroxyl groups, formation of hydrogen bonds between aromatic H atoms of the ligand and oxygen of sulfur dioxide (H^{δ+}...O^{δ-} interactions), interactions between open metal sites and oxygen of sulfur dioxide (M^{δ+}...O^{δ-} interactions), as well as interactions between sulfur and the carboxylate oxygen atoms of the ligand (S^{δ+}...O^{δ-} interactions).^{31,63–67}

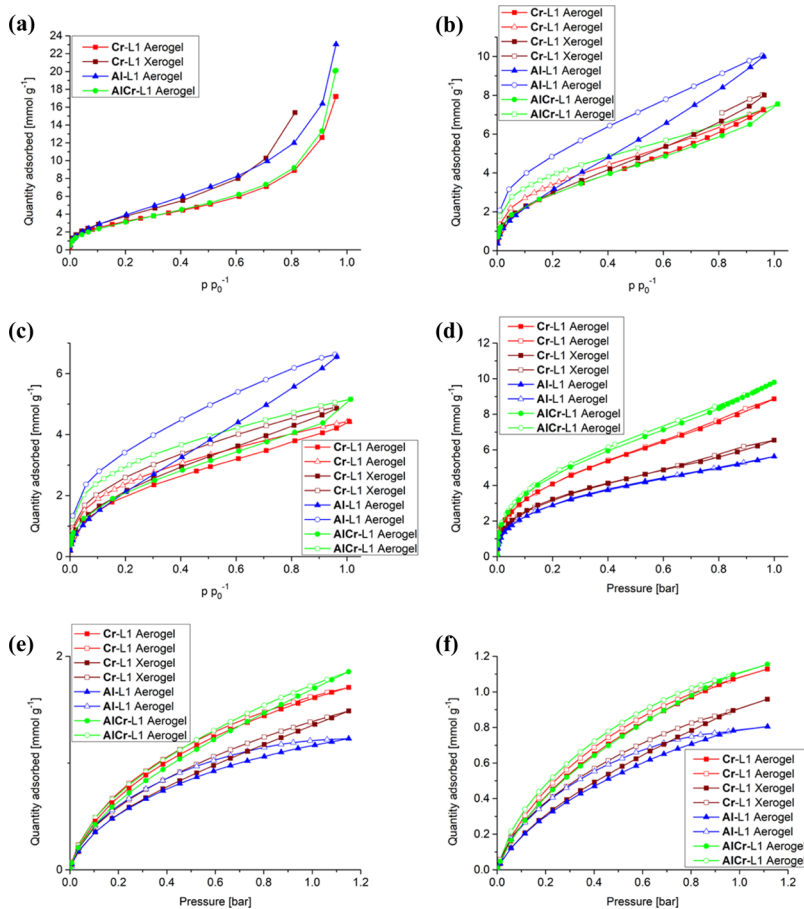


Figure 14. Adsorption (filled symbols) and desorption (empty symbols) isotherms for SO₂ and CO₂ on the synthesized materials at different temperatures. (a) SO₂ at 263 K, (b) SO₂ at 273 K, (c) SO₂ at 293 K, (d) CO₂ at 195 K, (e) CO₂ at 273 K, and (f) CO₂ at 293 K.

Table 3. Maximum Uptakes of CO₂ and SO₂ at 293 and 353 K for the Synthesized Materials

compound	max. uptake CO ₂ at 293 K [cm ³ g ⁻¹ , mmol g ⁻¹], exp.	max. uptake CO ₂ at 353 K [cm ³ g ⁻¹ , mmol g ⁻¹], calc.	max. uptake SO ₂ at 293 K [cm ³ g ⁻¹ , mmol g ⁻¹], exp.	max. uptake SO ₂ at 353 K [cm ³ g ⁻¹ , mmol g ⁻¹], calc.
Cr-L1 aerogel	24.0, 1.0	7.9, 0.3	116.8, 4.8	18.8, 0.8
Cr-L1 xerogel	21.5, 1.0	6.3, 0.3	109.5, 4.5	15.7, 0.6
AlCr-L1 aerogel	28.1, 1.2	7.3, 0.3	115.6, 4.7	27.0, 1.1
Al-L1 aerogel	19.8, 0.8	6.1, 0.3	146.8, 6.6	36.9, 1.5

Table 4. Comparison of SO₂ Uptake of Different Materials

compound	SO ₂ uptake [mmol g ⁻¹]	SO ₂ uptake [wt %]	pressure [bar]	temperature [K]	reference
Cr-L1 aerogel	4.8	23.4	1	293	this work
Cr-L1 xerogel	4.5	22.3	1	293	this work
AlCr-L1 aerogel	4.7	23.2	1	293	this work
Al-L1 aerogel	6.6	29.7	1	293	this work
NOTT-300 (MOF)	8.1	34.1	1	273	63
Mg-MOF-74	8.6	35.5	1.02	298	64
Ni(bdc)(ted) _{0.5} (MOF)	9.97	39.0	1.13	298	64
Zn ₂ (oxo-di-hbac) ₂ (bipy)	10.9	41.2	1	293	68
Na-MnO _x xerogel	1	6.0	1		16
Na-MnO _x aerogel	0.6	3.7	1		16
SiN-rGO aerogel	2.19	12.3	1	298	69

Uptake at Elevated Temperature and Breakthrough Curve Simulations. Existing applications for sorbent materials may not necessarily be at room temperature. In order to evaluate the materials for their uptake capacity at any temperature, the data obtained from the dual-site Langmuir isotherm fits recorded at different temperatures can be linearized against the measurement temperature. This circumvents possible device limitations, as many sorption devices do not allow measurements at elevated temperatures. For CO₂ sorption, the data often already exist, as measurements performed at 195 K are used for surface area determination, at 273 K for micropore evaluation and at 293 K for maximum uptake capacity at NTP. For SO₂ sorption, the temperature selection becomes a bit troublesome. SO₂ readily liquefies at 263 K, which in returns means that isotherms recorded at 293 K are just 30K above the boiling point. These isotherms still show pore condensation effects at higher partial pressures, as it can be seen in Figure 14. In order to fit these isotherms to the dual-site Langmuir model, data obtained above 0.5 *p* *p*₀⁻¹ have been neglected.

As expected, the isotherm fits of CO₂ are in good accordance with each other, making it possible to calculate isotherms at various temperatures (see Figure S20, Table S12).

For the SO₂ isotherms, the quality of fit was rather low. Possible reasons are, as stated above, condensation effects, which affect the dual-site Langmuir fit, or a possible degradation of the material by condensing SO₂. Only the materials containing Cr seem to have suffered from SO₂ exposure, as the quality of fit for the aerogel of Al-L1 stayed high throughout all measurements (Figure S21, Table S11). Table 3 contains the maximum uptake for CO₂ and SO₂ at 293 K as measured and 353 K as calculated and Table 4 shows a comparison to the maximum uptakes of some other aero- and xerogels, as well as MOFs.

While the metal–organic framework aerogels synthesized in this work are unable to compete with the best metal–organic frameworks when it comes to maximum SO₂ uptake, for

example, 6.6 mmol g⁻¹ for the aerogel of Al-L1, compared to 10.9 mmol g⁻¹ for Zn₂(oxo-di-hbac)₂(bipy), the MOF aerogels perform better than any known silica or metal oxide aerogel, with uptakes of 2.19 mmol g⁻¹ for a silica aerogel and 1 mmol g⁻¹ for a metal oxide aerogel.

Breakthrough curves have been calculated using the software 3P sim version 1.1.07, employing the “ideal adsorbed solution theory” (IAST) with data from fitted dual-site Langmuir isotherms.⁷⁰ The formula for the dual-site Langmuir isotherm is

$$m_{\text{eq}} = m_1 \frac{K_1 \times P}{1 + K_1 \times P} + m_2 \frac{K_2 \times P}{1 + K_2 \times P}$$

where m_{eq} is the loading at equilibrium, P the pressure, K_n the affinity constant, and m_n the maximal loading. The additional parameters used in the dual-site Langmuir isotherms compared to the Langmuir model allow for a greater degree of heterogeneity of adsorption sites in the material.⁷¹ The breakthrough curves were simulated at 20 °C under isothermal conditions. The percentage of CO₂ to SO₂ was taken from an article in which the exhaust gas composition of berthed marine vessels has been measured.⁷² The results for CO₂ and SO₂ were given in g kW h⁻¹, and the engine/fuel combination with the highest amount of SO₂ emission was chosen (9.6 g kW h⁻¹ SO₂, 697 g kW h⁻¹ CO₂, 5.57 vol % CO₂, SO₂/CO₂ ratio: 0.0138). The simulation for the exhaust gas composition therefore ran at the percentages of 5.57% CO₂ and 0.076% SO₂. Water has been neglected as a possible exhaust component, as other literature studies suggests that humidity only increases SO₂ uptake performance, but the large affinity for the materials to water would result in incorrect simulations.^{16,73} In recent literature, gas separation studies based on single-gas isotherms have been shown to be a convenient way to preselect an adsorbent materials for further evaluation, as they give a good indication of separation performance. For this interpretation, a prediction of mixture

equilibrium data based on pure component isotherms is required. It has been shown that the quality of the simulations, which were performed with a similar software, approaches the experimental breakthrough studies, as long as the separation is based on thermodynamic effects and not on kinetic-steric effects.⁷⁴

The simulation suggests that SO₂ is retained reasonably well for all materials except for the aerogel of Al-L1, which can of course be expected when considering the low affinity constant for SO₂ (Figure 15). To elaborate on that, the high total

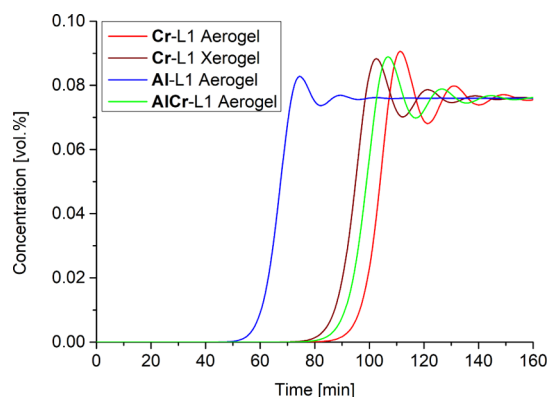


Figure 15. Simulated SO₂ breakthrough curves for the aero- and xerogels from a 1:73 v/v (0.076/5.57 vol %) SO₂/CO₂ gas mixture in an ideal inert gas. The CO₂ breakthrough curve is shown in Figure S22, Supporting Information. The retention time for Al-L1 is severely lacking, despite its high total uptake.

uptake for the Al-L1 aerogel is irrelevant for gas separation, as the uptake at low partial pressures is more decisive for the selectivity and therefore separation performance (Figure 16).

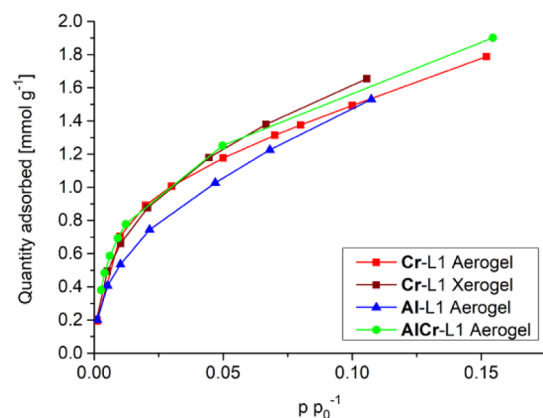


Figure 16. SO₂ isotherms at lower partial pressures. Despite the high maximum uptake of SO₂ on the aerogel of Al-L1, the uptake at lower partial pressures the least of the materials investigated here.

Table 5 lists the retention times for SO₂ and CO₂, as calculated by the software for the breakthrough simulations (cf. breakthrough curve simulation parameters and results in Supporting Information).

CONCLUSIONS

We were able to synthesize the new ligand *N*¹,*N*⁴-(diterephthalic acid)terephthalamide (H₄L1) and have successfully implemented it into new materials based on gel chemistry. The material based on Cr and H₄L1 exhibited

Table 5. Retention Times of the Synthesized Materials for the Breakthrough Simulations^a

compound	SO ₂	CO ₂
	retention time [min]	
Cr-L1 aerogel	102	2
Cr-L1 xerogel	93	1
AlCr-L1 aerogel	97	2
Al-L1 aerogel	66	1

^aFor details of the simulation, see breakthrough curve simulation parameters and results in Supporting Information.

excellent stability in its gel state and retained the shape even after conversion into its xero- and aerogel. Furthermore, in its metallogel state, it could successfully be utilized to selectively adsorb a dye from solution, which served as a model system for potential uptake of large molecules and pollutants from water. The Cr-based xero- and aerogel, combined with two additional aerogels based on Al and a mixture of Al and Cr, retain their porosity during the drying process, with large accessible surface areas. By putting the materials through a variety of physisorption experiments, the data derived from those experiments could be used to simulate breakthrough curves as well as the maximum uptake at elevated temperatures. The results show that the xero- and aerogels are able to filter a harmful gas, SO₂, from a gas mixture and that their maximum uptakes for this gas are the highest recorded for aerogels, rivaling uptakes of MOFs. In combination with their shapeability, these materials could be used as monolithic filter materials, unlike MOFs, which often have to be composited with a secondary material. The topic of MOAGs is often overlooked, although gels are sometimes an unwanted by-product of different synthesis strategies for new MOFs. This work demonstrates that there might be potential applications for gels based on metal–organic coordination chemistry. With supercritical drying becoming more prevalent in MOF workgroups as a way to dry porous materials without straining the framework, it should become more attractive to not discard metallogels and instead convert them into their xero- and aerogels and determine their usefulness in selective sorption applications.

EXPERIMENTAL SECTION

Materials and Methods. The chemicals used were of analytical grade obtained from commercial sources and used without further purification (see Table S3 in the Supporting Information for possible suppliers).

Fourier transform infrared spectra were measured in attenuated total reflection-mode (Platinum ATR-QL, Diamond) on a Bruker TENSOR 37 IR spectrometer in the range of 4000–600 cm⁻¹.

CHNS analysis was performed on a PerkinElmer CHN 2400.

Rheological characterization was performed with a DHR 3 Rheometer using a 40 mm plate geometry from TA Instruments to determine the mechanical properties. All measurements were performed at a constant axial force of 0.2 N at 25 °C. A frequency sweep (0.1–100 Hz) was performed at a constant strain of 0.3%, while an amplitude sweep was carried out at a constant frequency of 0.5 Hz and a strain of 0.1–100%.

Thermogravimetric analysis was performed on a Netzsch TG 209 F3 Tarsus in the range of 20–600 °C, equipped with Al-crucibles and applying a heat rate of 5 K min⁻¹ under nitrogen.

The powder X-ray diffraction patterns were obtained using a Bruker D2 Phaser powder diffractometer at 30 kV, 10 mA for Cu K α radiation ($\lambda = 1.51418 \text{ \AA}$).

Sorption Measurements. All sorption isotherms were determined on monolithic pieces of the materials. CO₂ sorption isotherms were measured with a Micromeritics ASAP 2020 gas sorption analyzer. The heat of adsorption values and BET surface areas were calculated using the ASAP 2020 v3.05 software. N₂ sorption isotherms were measured with Quantachrome Nova 4000e at 77 K. N₂ BET surface areas were calculated from the nitrogen adsorption isotherms using the NovaWin 11.03 software. Ar and SO₂ sorption isotherms were measured on a Quantachrome Autosorb IQ MP. Each SO₂ sorption run had to be completed within 6.5 h. This time limit was specified by the company Quantachrome to prevent damage to the gaskets. After this time, the system had to be regenerated by flushing with nitrogen. At the temperature of 263 K, which is the boiling point/condensation temperature of SO₂ at 1 bar, the sorption kinetics were so slow that only the adsorption isotherms could be completed in the given time limit. BET surface area and DFT calculations from argon sorption isotherms were performed using the ASiQwin 4.01 software. The pore size distributions were obtained using QSDFT calculations with an “Ar on carbon, slit pore” model, with the exception of the Al-L1 aerogel, where an “Ar on carbon, cylindrical pore” model has been used and no satisfying calculations could be performed with any other model. QSDFT calculations assume a greater degree of heterogeneity between adsorption sites compared to more standard nonlinear density functional theory (NLDFT) calculations, where each adsorption site is assumed to be equal. Water sorption isotherms have been measured on a Quantachrome VSTAR and have been evaluated using the VStarWin 1.1.15 software. All gases for the sorption measurements were of ultrapure grades (99.999%, 5.0), except for SO₂ (99.98%, 3.8), and the NTP volumes are given according to the NIST standards (293.15 K, 101.325 kPa). Helium gas was used for the determination of the cold and warm free space of the sample tubes. All samples have been degassed at 150 °C for at least 3 h prior to measurement. The fits of adsorption isotherms and the breakthrough curves have been calculated using the 3Psim 1.1.0.7 software by 3P Instruments GmbH & Co. KG.

Supercritical drying with CO₂ was performed on a Leica EM CPD300 using porous pots of pore sizes 120–200 μm. The solvent exchange has been performed at 10 °C for 99 cycles before heating to 50 °C and release of CO₂.

SEM images have been recorded with a JEOL JSM-6510LV QSEM advanced electron microscope equipped with a LaB₆ cathode. The microscope was equipped with a Bruker Xflash 410 silicon drift detector and Bruker ESPRIT software for EDX analysis. The samples were prepared for SEM microscopy by coating them with gold using a JEOL JFC 1200 fine-coater.

TEM images have been recorded with a Zeiss 902A electron microscope. The samples were prepared by suspending ground-up aerogel/xerogel in diethyl ether and dripping the suspension onto a carbon-coated copper grid and letting it dry. The TEM images have been edited to enlarge the scale bar. Unedited images can be found in the Supporting Information (Figure S12).

¹H NMR spectra were recorded with a Bruker Avance III 300 and 600 MHz.

Flame atomic absorption spectroscopy was performed with PerkinElmer PinAAcle 900T and evaluated using the Syngistix Software AA Version 3.0.

Synthesis of N¹,N⁴-(Diterephthalic acid)terephthalamide (H₄Ditatam, H₄L1). In a 500 mL round bottom flask, a mixture of 2.5 g (13.8 mmol) 2-aminoterephthalic acid and 8 g (57.88 mmol) potassium carbonate in 200 mL water was vigorously stirred until the 2-aminoterephthalic acid had dissolved. Terephthaloyl chloride (1.39 g; 6.83 mmol) was added; a cap was loosely put on the flask and it was stirred in a dark place for 5 days. The resulting mixture was carefully poured into 300 mL of 2M hydrochloric acid (being wary of foaming from excess potassium carbonate). The resulting suspension was filtered through a Büchner funnel and the funnel content was washed with water until the water ran off neutral. The resulting yellowish residue was suspended in 300 mL of dimethylformamide (DMF) and, under stirring, heated to 140 °C for 5 min. After letting the mixture cool down, the white solid was centrifuged off and the

DMF was decanted. The white solid was suspended in cold DMF and centrifuged off again. Afterward, this step was repeated three times with acetone instead of DMF. In vacuo dried at 80 °C, 1.00 g (2.03 mmol, 30%) was obtained. Elemental analysis calcd: C, 58.54; H, 3.28; N, 5.69. Found: C, 57.99; H, 3.50; N, 5.66. ¹H NMR (300 MHz, DMSO-*d*₆): δ 13.41 (s, 2-COOH), 12.19 (s, 2-NHCO-), 9.23 (s, 2=CH-), 8.16 (s, 4=CH-), 8.15 (d, *J* = 8.4 Hz, 2=CH-), 7.77 (dd, *J* = 1.70, 8.33, 2=CH-).

Suitable single crystals placed in viscous oil were carefully selected under a polarizing microscope and mounted in air onto a nylon loop. Crystallographic data and refinement details for the structure of H₄L1 are given in Table S1, Supporting Information. The structural data have been deposited with the Cambridge Crystallographic Data Center (CCDC no. 1889949).

Synthesis of Cr-L1 (Cr-Ditatam). H₄L1 (60.0 mg; 0.121 mmol) and 97.5 mg (0.242 mmol) of Cr(NO₃)₃·9H₂O (0.242 mmol) were added to a reaction vessel containing 5 mL DMF, sealed, and placed in an ultrasonic bath at 80 °C until the ligand had dissolved. The reaction vessel was transferred to an isothermal oven preheated to 80 °C. After 24 h, the gel was removed from the oven and left to cool. Elemental analysis calcd for aerogel of Cr₂-Ditatam·6H₂O·1DMF: C 41.65, H 4.04, N 5.43. Found: C 41.92, H 4.03, N 5.84. Karl Fischer titration calcd from EA, 16.2% H₂O; found, 10.8% H₂O.

Synthesis of Al-L1 (Al-Ditatam). H₄L1 (10.0 mg; 0.020 mmol) and 15.2 mg (0.041 mmol) Al(NO₃)₃·9H₂O, were added to a reaction vessel containing 5 mL of DMF, sealed, and placed in an ultrasonic bath at 80 °C until the ligand had dissolved. The reaction vessel was transferred to an isothermal oven preheated to 100 °C. After 24 h, the gel was removed from the oven and left to cool. Elemental analysis calcd for the aerogel of Al₂-Ditatam·7H₂O·0.5DMF: C 43.45, H 4.22, N 4.57. Found: C 43.28, H 4.13, N 4.66. Karl Fischer titration calcd from EA, 21.8% H₂O; found, 16.1%.

Synthesis of AlCr-L1 (AlCr-Ditatam). H₄L1 (20.0 mg; 0.041 mmol); 15.2 mg (0.041 mmol) Al(NO₃)₃·9H₂O; and 16.25 (0.041 mmol) Cr(NO₃)₃·9H₂O were added to a reaction vessel containing 5 mL DMF, sealed, and placed in an ultrasonic bath at 80 °C until the ligand had dissolved. The reaction vessel was transferred to an isothermal oven preheated to 100 °C. After 24 h, the gel was removed from the oven and left to cool. Elemental analysis calcd for the aerogel of AlCr-Ditatam·6.5H₂O·0.5DMF: C, 42.48; H, 3.98; N, 4.86. Found: C, 41.88; H, 3.78; N, 4.98. Karl Fischer titration calcd from EA, 19.4% H₂O; found, 13.6%.

Synthesis of the Cr-L1, AlCr-L1, and Al-L1 Aerogels. Pieces of the synthesized aerogels were directly transferred to macroporous specimen capsules with pore sizes of 120–200 μm. The capsules were put into a solvent exchange apparatus (Figure S24), in which they were kept for 5 days while continuously running the solvent exchange. Afterward, the capsules were removed from the apparatus and placed in a supercritical drying apparatus. After supercritical drying with CO₂, the aerogels were removed from the capsules.

Synthesis of the Cr-L1 Xerogel. The samples were prepared like the aerogels (solvent exchange), but underwent conventional vacuum drying at an elevated temperature (80 °C at 50 mbar) instead of supercritical drying.

Synthesis of In-L1 (In-Ditatam) and Fe-L1 (Fe-Ditatam). The synthesis of In-L1 and Fe-L1 was carried out analogous to the synthesis of Al-L1, using In(NO₃)₃·*x*H₂O and Fe(NO₃)₃·9H₂O instead as the metal salts. In(NO₃)₃·*x*H₂O was not previously dried, as drying the salt resulted in lower gel stability, and *x* = 6 was assumed for the stoichiometric calculations, as it provided the best results for the metallogel.

Synthesis of Hg-L1 (Hg-Ditatam). H₄L1 (10.0 mg; 0.02 mmol) was suspended in 4 mL of DMF and heated to 80 °C in a sonication bath. Mercury acetate (13.1 mg; 0.041 mmol), Hg(CH₃COO)₂, was dissolved in 1 mL of DMF in a separate vessel and also heated to 80 °C. After 1 h, the contents of both vessels were combined to instantly form the metallogel of Hg-L1.

Synthesis of Co-L1 (Co-Ditatam). H₄L1 (10.0 mg; 0.02 mmol) was dissolved in 4 mL of 25% ammonia solution. Hexamminecobalt chloride (11.0 mg; 0.041 mmol), [Co(NH₃)₆]Cl₃, was dissolved in 1

mL of 25% ammonia solution. The solutions were combined and the vessel was left open to let the ammonia evaporate. After ammonia evaporation, determined by olfactory analysis, the metallogel of Co-L1 had formed.

Dye Uptake Experiments. Cr-L1 metallogel (1 mL) was synthesized in a 5 mL vial, and 2 mL of aqueous dye solution with a concentration of 100 mg L⁻¹ was added to the vial. The vials were placed on a plate shaker at 250 rpm. The adsorption of the dyes was supposed to mainly happen at the interface between the gel and the dye solution, but in some cases the metallogel separated from the vial and therefore increased the solution–gel interface surface area. There was no measurable difference in equilibration time for those damaged gels.

■ ASSOCIATED CONTENT

Supporting Information

The Supporting Information is available free of charge on the ACS Publications website at DOI: 10.1021/acsami.9b04659.

Crystallographic data, reaction data, metallogel images, elemental and EDX analysis, IR spectra, PXRDs, SEM and TEM images, sorption data, dual-site Langmuir fitting data, breakthrough simulation parameters, H₄L1 NMR spectrum, solvent exchange apparatus, aerogel densities, and possible interactions contributing to dye uptake (PDF)

X-ray crystallographic data for compound H₄L1 [the structural data have also been deposited with the Cambridge Crystallographic Data Center (CCDC no. 1889949)] (CIF)

■ AUTHOR INFORMATION

Corresponding Author

*E-mail: janiak@uni-duesseldorf.de. Phone: +49 211 81 12286. Fax: +49 211 81 12287.

ORCID

Laura De Laporte: 0000-0002-9438-0977

Christoph Janiak: 0000-0002-6288-9605

Notes

The authors declare no competing financial interest.

■ ACKNOWLEDGMENTS

The research was funded in part by the German Science Foundation (DFG) through grant Ja466/29-1 and by the Federal German Ministry of Education and Research (BMBF) in the project Optimat under grant no. 03SF0492C. We thank the Center for Advanced Imaging and Stefan Kölzer of the Institut für Genetik of the Heinrich-Heine-Universität Düsseldorf for their support in obtaining the TEM images.

■ ABBREVIATIONS

BET, Brunauer–Emmett–Teller
DMF, dimethylformamide
IAST, idealized adsorbed solution theory
MOAG, metal–organic aerogel
MOF, metal–organic framework
NLDFT, nonlinear density functional theory
PXRD, powder X-ray diffractometry
SEM–EDX, scanning-electron microscopy–energy-dispersive X-ray spectroscopy
TEM, transmission electron microscopy
QSDF, quenched solid-state density functional theory

■ REFERENCES

- (1) Bobbitt, N. S.; Mendonca, M. L.; Howarth, A. J.; Islamoglu, T.; Hupp, J. T.; Farha, O. K.; Snurr, R. Q. Metal-organic frameworks for the removal of toxic industrial chemicals and chemical warfare agents. *Chem. Soc. Rev.* **2017**, *46*, 3357–3385.
- (2) Maurin, G.; Serre, C.; Cooper, A.; Férey, G. The New Age of MOFs and of their Porous-Related Solids. *Chem. Soc. Rev.* **2017**, *46*, 3104–3107.
- (3) Adil, K.; Belmabkhout, Y.; Pillai, R. S.; Cadiau, A.; Bhatt, P. M.; Assen, A. H.; Maurin, G.; Eddaoudi, M. Gas/vapour separation using ultra-microporous metal-organic frameworks: insights into the structure/separation relationship. *Chem. Soc. Rev.* **2017**, *46*, 3402–3430.
- (4) Zhang, T.; Hu, Y.-Q.; Han, T.; Zhai, Y.-Q.; Zheng, Y.-Z. Redox-Active Cobalt(II/III) Metal-Organic Framework for Selective Oxidation of Cyclohexene. *ACS Appl. Mater. Interfaces* **2018**, *10*, 15786–15792.
- (5) Li, J.-R.; Sculley, J.; Zhou, H.-C. Metal-Organic Frameworks for Separations. *Chem. Rev.* **2012**, *112*, 869–932.
- (6) Lei, B.; Wang, M.; Jiang, Z.; Qi, W.; Su, R.; He, Z. Constructing Redox-Responsive Metal-Organic Framework Nanocarriers for Anticancer Drug Delivery. *ACS Appl. Mater. Interfaces* **2018**, *10*, 16698–16706.
- (7) Pankajakshan, A.; Sinha, M.; Ojha, A. A.; Mandal, S. Water-Stable Nanoscale Zirconium-Based Metal-Organic Frameworks for the Effective Removal of Glyphosate from Aqueous Media. *ACS Omega* **2018**, *3*, 7832–7839.
- (8) Su, X.; Bromberg, L.; Martis, V.; Simeon, F.; Huq, A.; Hatton, T. A. Postsynthetic Functionalization of Mg-MOF-74 with Tetraethylenepentamine: Structural Characterization and Enhanced CO₂ Adsorption. *ACS Appl. Mater. Interfaces* **2017**, *9*, 11299–11306.
- (9) Bonnefoy, J.; Legrand, A.; Quadrelli, E. A.; Canivet, J.; Farrusseng, D. Enantiopure Peptide-Functionalized Metal-Organic Frameworks. *J. Am. Chem. Soc.* **2015**, *137*, 9409–9416.
- (10) El-Kaderi, H. M.; Hunt, J. R.; Mendoza-Cortes, J. L.; Cote, A. P.; Taylor, R. E.; O’Keeffe, M.; Yaghi, O. M. Designed Synthesis of 3D Covalent Organic Frameworks. *Science* **2007**, *316*, 268–272.
- (11) Kitao, T.; Zhang, Y.; Kitagawa, S.; Wang, B.; Uemura, T. Hybridization of MOFs and Polymers. *Chem. Soc. Rev.* **2017**, *46*, 3108–3133.
- (12) Wickenheisser, M.; Herbst, A.; Tannert, R.; Milow, B.; Janiak, C. Hierarchical MOF-xerogel Monolith Composites from Embedding MIL-100(Fe,Cr) and MIL-101(Cr) in Resorcinol-Formaldehyde Xerogels for Water Adsorption Applications. *Micropor. Mesopor. Mater.* **2015**, *215*, 143–153.
- (13) Wickenheisser, M.; Paul, T.; Janiak, C. Prospects of Monolithic MIL-MOF@poly(NIPAM)HIPE Composites as Water Sorption Materials. *Micropor. Mesopor. Mater.* **2016**, *220*, 258–269.
- (14) Maldonado-Hódar, F. J.; Ferro-García, M. A.; Rivera-Utrilla, J.; Moreno-Castilla, C. Synthesis and Textural Characteristics of Organic Aerogels, Transition-Metal-Containing Organic Aerogels and their Carbonized Derivatives. *Carbon* **1999**, *37*, 1199–1205.
- (15) Hirst, A. R.; Escuder, B.; Miravet, J. F.; Smith, D. K. High-Tech Applications of Self-Assembling Supramolecular Nanostructured Gel-Phase Materials: From Regenerative Medicine to Electronic Devices. *Angew. Chem., Int. Ed.* **2008**, *47*, 8002–8018.
- (16) Long, J. W.; Wallace, J. M.; Peterson, G. W.; Huynh, K. Manganese Oxide Nanoarchitectures as Broad-Spectrum Sorbents for Toxic Gases. *ACS Appl. Mater. Interfaces* **2016**, *8*, 1184–1193.
- (17) Kistler, S. S. Coherent Expanded Aerogels and Jellies. *Nature* **1931**, *127*, 741.
- (18) Maleki, H.; Durães, L.; Portugal, A. An Overview on Silica Aerogels Synthesis and Different Mechanical Reinforcing Strategies. *J. Non-Cryst. Solids* **2014**, *385*, 55–74.
- (19) Kumar, A.; Rana, A.; Sharma, G.; Sharma, S.; Naushad, M.; Mola, G. T.; Dhiman, P.; Stadler, F. J. Aerogels and Metal-Organic Frameworks for Environmental Remediation and Energy Production. *Environ. Chem. Lett.* **2018**, *16*, 797–820.

- (20) Pierre, A. C.; Pajonk, G. M. Chemistry of Aerogels and their Applications. *Chem. Rev.* **2002**, *102*, 4243–4266.
- (21) Hüsing, N.; Schubert, U. Aerogels-Airy Materials: Chemistry, Structure, and Properties. *Angew. Chem., Int. Ed.* **1998**, *37*, 22–45.
- (22) Soleimani Dorcheh, A.; Abbasi, M. H. Silica Aerogel; Synthesis, Properties and Characterization. *J. Mater. Process. Technol.* **2008**, *199*, 10–26.
- (23) Lohe, M. R.; Rose, M.; Kaskel, S. Metal-Organic Framework (MOF) Aerogels with High Micro- and Macroporosity. *Chem. Commun.* **2009**, 6056–6058.
- (24) Tam, A. Y.-Y.; Yam, V. W.-W. Recent Advances in Metallogels. *Chem. Soc. Rev.* **2013**, *42*, 1540–1567.
- (25) Sutar, P.; Maji, T. K. Coordination Polymer Gels: Soft Metal-Organic Supramolecular Materials and Versatile Applications. *Chem. Commun.* **2016**, *52*, 8055–8074.
- (26) Li, L.; Xiang, S.; Cao, S.; Zhang, J.; Ouyang, G.; Chen, L.; Su, C.-Y. A Synthetic Route to Ultralight Hierarchically Micro/Mesoporous Al(III)-Carboxylate Metal-Organic Aerogels. *Nat. Commun.* **2013**, *4*, 1774.
- (27) Xia, W.; Zhang, X.; Xu, L.; Wang, Y.; Lin, J.; Zou, R. Facile and Economical Synthesis of Metal-Organic Framework MIL-100(Al) Gels for High Efficiency Removal of Microcystin-LR. *RSC Adv.* **2013**, *3*, 11007–11013.
- (28) Saraji, M.; Shahvar, A. Metal-organic aerogel as a coating for solid-phase microextraction. *Anal. Chim. Acta* **2017**, *973*, 51–58.
- (29) Albo, J.; Vallejo, D.; Beobide, G.; Castillo, O.; Castaño, P.; Irabien, A. Copper-Based Metal-Organic Porous Materials for CO₂ Electrocatalytic Reduction to Alcohols. *ChemSusChem* **2017**, *10*, 1100–1109.
- (30) Han, X.; Yang, S.; Schröder, M. Porous metal-organic frameworks as emerging sorbents for clean air. *Nat. Rev. Chem.* **2019**, *3*, 108–118.
- (31) Zhang, Y.; Zhang, P.; Yu, W.; Zhang, J.; Huang, J.; Wang, J.; Xu, M.; Deng, Q.; Zeng, Z.; Deng, S. Highly Selective and Reversible Sulfur Dioxide Adsorption on a Microporous Metal-Organic Framework via Polar Sites. *ACS Appl. Mater. Interfaces* **2019**, *11*, 10680–10688.
- (32) Lee, J.-Y.; Keener, T. C.; Yang, Y. J. Potential Flue Gas Impurities in Carbon Dioxide Streams Separated from Coal-Fired Power Plants. *Air Waste Manage. Assoc.* **2012**, *59*, 725–732.
- (33) Srivastava, R. K.; Jozewicz, W. Flue Gas Desulfurization: The State of the Art. *Air Waste Manage. Assoc.* **2011**, *51*, 1676–1688.
- (34) Rall, D. P. Review of the Health Effects of Sulfur Oxides. *Environ. Health Perspect.* **1974**, *8*, 97–121.
- (35) Gregory, K.; Webster, C.; Durk, S. Estimates of Damage to Forests in Europe due to Emissions of Acidifying Pollutants. *Energy Pollut.* **1996**, *24*, 655–664.
- (36) Likens, G. E.; Driscoll, C. T.; Buso, D. C. Long-Term Effects of Acid Rain: Response and Recovery of a Forest Ecosystem. *Science* **1996**, *272*, 244–246.
- (37) Nakamoto, K. *Infrared and Raman Spectra of Inorganic and Coordination Compounds*, 3rd ed.; Wiley-Interscience: New York, 1978.
- (38) Deacon, G.; Phillips, R. J. Relationships Between the Carbon-Oxygen Stretching Frequencies of Carboxylate Complexes and the Type of Carboxylate Coordination. *Coord. Chem. Rev.* **1980**, *33*, 227–250.
- (39) Dastidar, P.; Ganguly, S.; Sarkar, K. Metallogels from Coordination Complexes, Organometallic, and Coordination Polymers. *Chem.—Asian. J.* **2016**, *11*, 2484–2498.
- (40) Piepenbrock, M.-O. M.; Lloyd, G. O.; Clarke, N.; Steed, J. W. Metal- and anion-binding supramolecular gels. *Chem. Rev.* **2010**, *110*, 1960–2004.
- (41) Vallejo-Sánchez, D.; Amo-Ochoa, P.; Beobide, G.; Castillo, O.; Fröba, M.; Hoffmann, F.; Luque, A.; Ocón, P.; Pérez-Yáñez, S. Chemically Resistant, Shapeable, and Conducting Metal-Organic Gels and Aerogels Built from Dithiooxamidato Ligand. *Adv. Funct. Mater.* **2017**, *27*, 1605448.
- (42) Serre, C.; Millange, F.; Thouvenot, C.; Noguès, M.; Marsolier, G.; Louër, D.; Férey, G. Very Large Breathing Effect in the First Nanoporous Chromium(III)-Based Solids: MIL-53 or CrIII(OH)-{O₂C–C₆H₄–CO₂}₂{HO₂C–C₆H₄–CO₂H}_xH₂O_y. *J. Am. Chem. Soc.* **2002**, *124*, 13519–13526.
- (43) Loiseau, T.; Serre, C.; Huguenard, C.; Fink, G.; Taulelle, F.; Henry, M.; Bataille, T.; Férey, G. A Rationale for the Large Breathing of the Porous Aluminum Terephthalate (MIL-53) Upon Hydration. *Chemistry* **2004**, *10*, 1373–1382.
- (44) Reinsch, H.; van der Veen, M. A.; Gil, B.; Marszałek, B.; Verbiest, T.; de Vos, D.; Stock, N. Structures, Sorption Characteristics, and Nonlinear Optical Properties of a New Series of Highly Stable Aluminum MOFs. *Chem. Mater.* **2012**, *25*, 17–26.
- (45) Alvarez, E.; Guillou, N.; Martineau, C.; Bueken, B.; Van de Voorde, B.; Le Guillouzer, C.; Fabry, P.; Nouar, F.; Taulelle, F.; de Vos, D.; Chang, J.-S.; Cho, K. H.; Ramsahye, N.; Devic, T.; Daturi, M.; Maurin, G.; Serre, C. The Structure of the Aluminum Fumarate Metal-Organic Framework AS20. *Angew. Chem., Int. Ed. Engl.* **2015**, *54*, 3664–3668.
- (46) Zhao, X.; Yuan, L.; Zhang, Z.-q.; Wang, Y.-s.; Yu, Q.; Li, J. Synthetic Methodology for the Fabrication of Porous Porphyrin Materials with Metal-Organic-Polymer Aerogels. *Inorg. Chem.* **2016**, *55*, 5287–5296.
- (47) Xiang, S.; Li, L.; Zhang, J.; Tan, X.; Cui, H.; Shi, J.; Hu, Y.; Chen, L.; Su, C.-Y.; James, S. L. Porous Organic–Inorganic Hybrid Aerogels Based on Cr³⁺/Fe³⁺ and Rigid Bridging Carboxylates. *J. Mater. Chem.* **2012**, *22*, 1862–1867.
- (48) International Agency for Research on Cancer. IARC Monographs on the Evaluation of Carcinogenic Risks to Humans. List of Classifications, Vols. 1–123. <https://monographs.iarc.fr/list-of-classifications-volumes/> (accessed March 10, 2019).
- (49) Furry, J. W. Preparation, properties and applications of Calcein in a highly pure form. Retrospective Theses and Dissertations, 1985, p 12062.
- (50) <https://www.thermofisher.com/order/catalog/product/22858> (accessed March 10, 2019).
- (51) Brown, D. Effects of colorants in the aquatic environment. *Ecotoxicol. Environ. Saf.* **1987**, *13*, 139–147.
- (52) Farré, M. I.; Pérez, S.; Kantiani, L.; Barceló, D. Fate and toxicity of emerging pollutants, their metabolites and transformation products in the aquatic environment. *Trends Anal. Chem.* **2008**, *27*, 991–1007.
- (53) El Haddad, M. Removal of Basic Fuchsin Dye from Water Using Mussel Shell Biomass Waste as an Adsorbent: Equilibrium, Kinetics, and Thermodynamics. *J. Taibah Univ. Sci.* **2018**, *10*, 664–674.
- (54) Song, Y. H.; Chen, S. M.; Ren, J. M.; Gao, Y.; Xu, H. Fuchsin Adsorption from Aqueous Solution by Epichlorohydrin Crosslinked Peanut Husk. *Adv. Mater. Res.* **2012**, *549*, 362–365.
- (55) Jedynak, K.; Repelewicz, M. Adsorption of Acid Red 114 and Basic Fuchsin from Aqueous Solutions on Mesoporous Carbon Materials. *Environ. Prot. Eng.* **2016**, *19*, 227–239.
- (56) Yan, S.; Pan, Y.; Wang, L.; Liu, J.; Zhang, Z.; Huo, W.; Yang, J.; Huang, Y. Synthesis of Low-Cost Porous Ceramic Microspheres from Waste Gangue for Dye Adsorption. *J. Adv. Ceram.* **2017**, *7*, 30–40.
- (57) Gupta, V. K.; Mittal, A.; Gajbe, V.; Mittal, J. Adsorption of basic fuchsin using waste materials-bottom ash and deoiled soya-as adsorbents. *J. Colloid Interface Sci.* **2008**, *319*, 30–39.
- (58) Tran, H. N.; Wang, Y.-F.; You, S.-J.; Chao, H.-P. Insights into the mechanism of cationic dye adsorption on activated charcoal: The importance of π - π interactions. *Process Saf. Environ. Prot.* **2017**, *107*, 168–180.
- (59) Thommes, M.; Kaneko, K.; Neimark, A. V.; Olivier, J. P.; Rodriguez-Reinoso, F.; Rouquerol, J.; Sing, K. S. W. Physisorption of Gases, with Special Reference to the Evaluation of Surface Area and Pore Size Distribution (IUPAC Technical Report). *Pure Appl. Chem.* **2015**, *87*, 1051–1069.
- (60) Yang, Q.; Tan, X.; Wang, S.; Zhang, J.; Chen, L.; Zhang, J.-P.; Su, C.-Y. Porous organic-inorganic hybrid aerogels based on bridging acetylacetonate. *Micropor. Mesopor. Mater.* **2014**, *187*, 108–113.

(61) Low, J. J.; Benin, A. I.; Jakubczak, P.; Abrahamian, J. F.; Faheem, S. A.; Willis, R. R. Virtual High Throughput Screening Confirmed Experimentally: Porous Coordination Polymer Hydration. *J. Am. Chem. Soc.* **2009**, *131*, 15834–15842.

(62) Leus, K.; Bogaerts, T.; De Decker, J.; Depauw, H.; Hendrickx, K.; Vrielinck, H.; Van Speybroeck, V.; Van Der Voort, P. Systematic study of the chemical and hydrothermal stability of selected "stable" Metal Organic Frameworks. *Micropor. Mesopor. Mater.* **2016**, *226*, 110–116.

(63) Yang, S.; Sun, J.; Ramirez-Cuesta, A. J.; Callear, S. K.; David, W. I. F.; Anderson, D. P.; Newby, R.; Blake, A. J.; Parker, J. E.; Tang, C. C.; Schröder, M. Selectivity and Direct Visualization of Carbon Dioxide and Sulfur Dioxide in a Decorated Porous Host. *Nat. Chem.* **2012**, *4*, 887–894.

(64) Tan, K.; Canepa, P.; Gong, Q.; Liu, J.; Johnson, D. H.; Dyevoich, A.; Thallapally, P. K.; Thonhauser, T.; Li, J.; Chabal, Y. J. Mechanism of Preferential Adsorption of SO₂ into Two Microporous Paddle Wheel Frameworks M(bdc)(ted)0.5. *Chem. Mater.* **2013**, *25*, 4653–4662.

(65) Li, L.; da Silva, I.; Kolokolov, D. I.; Han, X.; Li, J.; Smith, G.; Cheng, Y.; Daemen, L. L.; Morris, C. G.; Godfrey, H. G. W.; Jacques, N. M.; Zhang, X.; Manuel, P.; Frogley, M. D.; Murray, C. A.; Ramirez-Cuesta, A. J.; Cinque, G.; Tang, C. C.; Stepanov, A. G.; Yang, S.; Schroder, M. Post-Synthetic Modulation of the Charge Distribution in a Metal-Organic Framework for Optimal Binding of Carbon Dioxide and Sulfur Dioxide. *Chem. Sci.* **2019**, *10*, 1472–1482.

(66) Tan, K.; Zuluaga, S.; Wang, H.; Canepa, P.; Soliman, K.; Cure, J.; Li, J.; Thonhauser, T.; Chabal, Y. J. Interaction of Acid Gases SO₂ and NO₂ with Coordinatively Unsaturated Metal Organic Frameworks: M-MOF-74 (M = Zn, Mg, Ni, Co). *Chem. Mater.* **2017**, *29*, 4227–4235.

(67) Brandt, P.; Nuhnen, A.; Lange, M.; Möllmer, J.; Weingart, O.; Janiak, C. Metal–Organic Frameworks with Potential Application for SO₂ Separation and Flue Gas Desulfurization. *ACS Appl. Mater. Interfaces* **2019**, *11*, 17350–17358.

(68) Glomb, S.; Woschko, D.; Makhlofi, G.; Janiak, C. Metal-Organic Frameworks with Internal Urea-Functionalized Dicarboxylate Linkers for SO₂ and NH₃ Adsorption. *ACS Appl. Mater. Interfaces* **2017**, *9*, 37419–37434.

(69) Yun, S.; Kim, H.; Lee, H.; Park, H. S. Three-Dimensionally Macroporous, Si and N-Incorporated Graphene Aerogels for Gas Adsorbents. *Mater. Express* **2015**, *5*, 463–469.

(70) Myers, A. L.; Prausnitz, J. M. Thermodynamics of Mixed-Gas Adsorption. *AIChE J.* **1965**, *11*, 121–127.

(71) Mathias, P. M.; Kumar, R.; Moyer, J. D., Jr.; Schork, J. M.; Srinivasan, S. R.; Auvil, S. R.; Talu, O. Correlation of Multicomponent Gas Adsorption by the Dual-Site Langmuir Model. Application to Nitrogen/Oxygen Adsorption on 5A-Zeolite. *Ind. Eng. Chem. Res.* **1996**, *35*, 2477–2483.

(72) Cooper, D. Exhaust Emissions From Ships at Berth. *Atmos. Environ.* **2003**, *37*, 3817–3830.

(73) Peterson, G. W.; Karwacki, C. J.; Feaver, W. B.; Rossin, J. A. Zirconium Hydroxide as a Reactive Substrate for the Removal of Sulfur Dioxide. *Ind. Eng. Chem. Res.* **2009**, *48*, 1694–1698.

(74) Möller, A.; Eschrich, R.; Reichenbach, C.; Guderian, J.; Lange, M.; Möllmer, J. Dynamic and Equilibrium-Based Investigations of CO₂-Removal from CH₄-Rich Gas Mixtures on Microporous Adsorbents. *Adsorption* **2016**, *23*, 197–209.